

OMGSR: You Only Need One Mid-timestep Guidance for Real-World Image Super-Resolution

Zhiqiang Wu^{1,2*} Zhaomang Sun² Tong Zhou² Bingtao Fu² Ji Cong²
Yitong Dong² Huaqi Zhang² Xuan Tang¹ Mingsong Chen¹ Xian Wei^{1†}
¹East China Normal University ²vivo Mobile Communication Co., Ltd.

Abstract

Denoising Diffusion Probabilistic Models (DDPMs) show promising potential in one-step Real-World Image Super-Resolution (Real-ISR). Current one-step Real-ISR methods typically inject the low-quality (LQ) image latent representation at the start or end timestep of the DDPM scheduler. Recent studies have begun to note that the LQ image latent and the pre-trained noisy latent representations are intuitively closer at a mid-timestep. However, a quantitative analysis of these latent representations remains lacking. Considering these latent representations can be decomposed into signal and noise, we propose a method based on the Signal-to-Noise Ratio (SNR) to pre-compute an average optimal mid-timestep for injection. To better approximate the pre-trained noisy latent representation, we further introduce the Latent Representation Refinement (LRR) loss via a LoRA-enhanced VAE encoder. We also fine-tune the backbone of the DDPM-based generative model using LoRA to perform one-step denoising at the average optimal mid-timestep. Based on these components, we present OMGSR, a GAN-based Real-ISR framework that employs a DDPM-based generative model as the generator and a DINOv3-ConvNeXt model with multi-level discriminator heads as the discriminator. We also propose the DINOv3-ConvNeXt DISTs (Dv3CD) loss, which is enhanced for structural perception at varying resolutions. Within the OMGSR framework, we develop OMGSR-S based on SD2.1-base. An ablation study confirms that our pre-computation strategy and LRR loss significantly improve the baseline. Comparative studies demonstrate that OMGSR-S achieves state-of-the-art performance across multiple metrics. Code is available at <https://github.com/wuer5/OMGSR>.

1. Introduction

Image Super-Resolution (ISR) [25, 44, 50] aims to reconstruct High-Quality (HQ) images from Low-Quality

*Work done during internship at vivo. †Corresponding author.

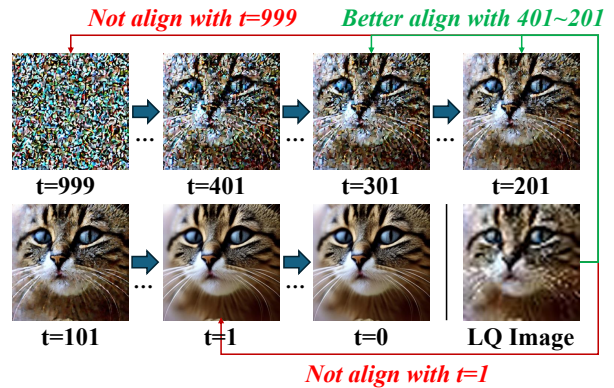


Figure 1. Illustration of a 20-step inference process with the prompt (*i.e.* a cute cat) in SD2.1-base DDPM. We decode the latent representations into images at each step. The LQ image is sampled from the RealESRGAN degradation pipeline.

(LQ) inputs, with applications in image and face restoration [23, 40, 60]. Recent work focuses on Real-World ISR (Real-ISR) [3, 28], where degradation patterns are complex and unknown. While training ISR models requires paired LQ-HQ data, collecting real-world LQ degraded images is challenging. Thus, synthetic degradation pipelines such as BSRGAN [55] and Real-ESRGAN [41] are widely used to approximate realistic degradation.

However, synthetic LQ images often deviate from real-world representations, limiting the generalization ability of models trained on such data. Traditional supervised methods [7, 18, 31] perform well on synthetic pairs but struggle with real-world images due to insufficient priors [38].

Recent advances widely leverage large-scale pre-trained generative models (*e.g.* Stable Diffusion (SD) [29]) to fit the Real-ISR tasks due to their rich image priors [16, 39]. Models like StableSR [38], DiffBIR [20] exploit the rich priors of these foundation models, which offer stronger generalization on Real-ISR tasks and stable training via efficient fine-tuning techniques such as LoRA [12] and ControlNet [56].

Despite their success, these methods suffer from slow

inference due to the multi-step denoising process. Recent one-step models, such as SinSR [42] and OSEDiff [46], significantly reduce inference time by distilling knowledge into a one step. These methods commonly encode LQ images into their latent representations, process them with a UNet [30] for one-step denoising, and decode the output with reconstruction losses [26] or other knowledge distillation techniques [10].

Although one-step methods have made notable advancements, we observe that existing models (*e.g.* OSEDiff [46] and PiSA-SR [35]) typically inject the LQ image latent representation into the UNet in an SD model at the start ($t = 999$) or end ($t = 1$) timestep, creating a latent representation gap. As illustrated in Fig. 1, we decode the latent representations into the corresponding images in a 20-step inference process for SD2.1-base [29]. The figure shows that LQ images align significantly more closely with images at the mid-timestep than with those at the start or end timestep. **This finding suggests that taking the LQ image latent representation as the input at a mid-timestep would narrow the latent representation gap.**

The most recent work, InvSR [54], has considered this gap and set a series of mid-timesteps (*e.g.* 250, 200, 150, 100, and 50) based on experience. However, he neither quantitatively analyzed the mid-timesteps from the perspective of pre-training nor further narrowed this gap from the parameter training standpoint.

Based on this observation and motivation, this work focuses on narrowing the gap between the LQ image latent representations and the pre-trained noisy latent representations. **We make the following contributions:**

- We introduce the Signal-to-Noise Ratio (SNR) based method to pre-compute an optimal mid-timestep for injection in DDPM-based generative models.
- To further reduce the latent representation gap, we propose the Latent Representation Refinement (LRR) loss, implemented via fine-tuning the VAE encoder with LoRA to approach the pre-trained noisy latent representation.
- We present OMGSR, a universal GAN-based Real-ISR framework compatible with DDPM-based generative models. In this framework, a generative model (LoRA-trainable) serves as the generator, while a DINOv3-ConvNeXt (frozen) with a multi-level discriminator (fully trainable) constitutes the discriminator.
- We propose the DINOv3-ConvNeXt DISTS (Dv3CD) loss to enhance structural perception, addressing the resolution mismatch between a model’s native resolution and the Real-ISR task’s requirements, a discrepancy that often leads to artifacts. The Dv3CD loss natively supports training at high resolutions, such as 512, 1K, and beyond.
- Under the OMGSR framework, we develop OMGSR-S (SD2.1-base), which achieves state-of-the-art performance across multiple benchmark metrics.

2. Related Work

2.1. Multi-step Real-ISR Models

Recent studies have employed advanced pre-trained text-to-image (T2I) models, such as SD-based generative models [29], to address challenges in Real-ISR. StableSR [38] leverages generative priors from SD2.1-base for Real-ISR, using a time-aware encoder and controllable feature wrapping to restore HQ images. SeeSR [47] utilizes high-quality semantic prompts to enhance the generative capacity of the SD2-base. DiffBIR [20] proposes IRControlNet, which leverages the image priors of the SD2.1-base model for Real-ISR. Other multi-step Real-ISR models, such as PASD [49], ResShift [53], and SUPIR [51], also leverage powerful SD priors to achieve excellent results.

2.2. One-step Real-ISR Models

Although multi-step Real-ISR models have achieved considerable success, their major drawback is their slow inference speed. Generally, an N -step model requires approximately N times the inference time of a one-step model, a critical limitation. In addition, multi-step models tend to be more generative, and their fidelity in Real-ISR tasks is also a challenge.

Thus, one-step models have become a primary research focus in recent years due to the fast speed and high fidelity, making them suitable for Real-ISR tasks. OSEDiff [46] enables one-step Real-ISR by directly diffusing from the LQ image, eliminating random noise uncertainty while maintaining high-quality output through variational score distillation to conduct KL-divergence regularization. SinSR [42] achieves one-step Real-ISR by distilling a multi-step diffusion model into a student network through deterministic mapping and a novel consistency-preserving loss. PiSA-SR [35] introduces a decoupled LoRA module for pixel-accurate and semantic-aware Real-ISR, enabling one-step, adjustable quality-fidelity trade-offs without retraining.

2.3. Timestep for Injection

For multi-step models, the majority perform multi-step denoising starting from the initial timestep (*i.e.* 999), following a similar training and inference process as the original SD. In contrast, one-step models typically inject the LQ image latent representation into the UNet in an SD model at specific timesteps. For instance, OSEDiff [46] injects at timestep 999, while PiSA-SR [35] injects at timestep 1. However, in pre-training, timestep 999 corresponds to Gaussian noise, whereas timestep 1 corresponds to a clean image, leading to a latent representation gap. In fact, the pre-trained noisy latent representation at mid-timesteps in SD is closer to the LQ image latent representation.

The most recent work, InvSR [54], has considered this by empirically selecting a series of mid-timesteps for in-

jecting the LQ image latent representation, thereby reducing the latent representation gap. Moreover, InvSR supports both one-step and multi-step inference by choosing one or multiple mid-timesteps.

Nevertheless, the selection of mid-timesteps in InvSR relies on empirical manual settings, without quantifying the selection process or further comparing the pre-trained noisy latent representation from a parameter-optimization perspective. To address this limitation, this paper explores this direction, aiming to bring the LQ image latent representation closer to the pre-trained noisy latent representation.

3. Methodology

In this section, we define: \mathbf{x}_L and \mathbf{x}_H as the LQ image and HQ image, \mathbf{z}_L and \mathbf{z}_H as their corresponding latent representations, \mathbf{z}_t as the pre-trained noisy latent representation at timestep t , where $t \in \{1, \dots, T\}$, \mathcal{E} and \mathcal{D} are VAE encoder and decoder, respectively.

3.1. Preliminary

Denoising Diffusion Probabilistic Models (DDPM [11]). Define variances $\{\beta_1, \beta_2, \dots, \beta_T\}$, $\alpha_t = \prod_{s=1}^t (1 - \beta_s)$, the pre-trained noisy latent representation \mathbf{z}_t can be combined linearly by HQ image latent representation \mathbf{z}_H and Gaussian noise $\epsilon \sim \mathcal{N}(0, I)$ via a noise-added process:

$$\mathbf{z}_t = \sqrt{\alpha_t} \cdot \mathbf{z}_H + \sqrt{1 - \alpha_t} \cdot \epsilon, \quad (1)$$

where $\mathbf{z}_{999} \approx \epsilon$ and $\mathbf{z}_1 \approx \mathbf{z}_H$. In pre-training, the DDPM-based models (e.g. SD2.1-base) typically use $T = 999$. The pre-trained noisy latent representation \mathbf{z}_t , timestep t , and conditions c (e.g. prompt embeddings) are input into the UNet ϵ_θ to predict a noise. The DDPM training objective loss is

$$\mathcal{L}_{\text{DDPM}} = \|\epsilon_\theta(\mathbf{z}_t, t, c) - \epsilon\|_2^2. \quad (2)$$

3.2. Motivation: Latent Representation Gap

One-step SD-based Real-ISR models (e.g. OSEDiff [46] or PiSA-SR [35]) fine-tune the UNet [30] in SD2.1-base by directly feeding the LQ image latent representation \mathbf{z}_L at initial timestep 999 or end timestep 1 *i.e.* they assume that $\mathbf{z}_{999} = \mathbf{z}_L$ or $\mathbf{z}_1 = \mathbf{z}_L$. However, such assumptions create a fundamental gap since $\mathbf{z}_{999} = \epsilon$ or $\mathbf{z}_1 = \mathbf{z}_H$ according to Eq. 1. In fact, $\mathbf{z}_L \neq \epsilon$ or $\mathbf{z}_L \neq \mathbf{z}_H$ in Real-ISR tasks.

Recent studies, such as InvSR [54], have noted this problem, but they fail to quantify this gap and instead roughly select a series of mid-timesteps based on experience. We focus on quantifying this selection process and further narrowing the latent representation gap.

3.3. Pre-computed Mid-timestep

3.3.1. Signal-to-Noise Ratio (SNR)

DDPM-based models involve a pre-trained noisy latent representation \mathbf{z}_t at timestep t , which is a linear combination

of Gaussian noise ϵ and the HQ image latent representation \mathbf{z}_H . The SNR of \mathbf{z}_t is:

$$\text{SNR}(\mathbf{z}_t) = \frac{\bar{\alpha}_t \cdot \mathbb{E}[\mathbf{z}_H^2]}{(1 - \bar{\alpha}_t) \cdot \mathbb{E}[\epsilon^2]} = \frac{\bar{\alpha}_t \cdot \mathbb{E}[\mathbf{z}_H^2]}{1 - \bar{\alpha}_t} \quad (3)$$

where $\epsilon \sim \mathcal{N}(0, I)$ and $\mathbb{E}[\epsilon^2] = 1$.

Similarly, LQ images are obtained by applying a series of degradation processes to HQ images, where \mathbf{z}_L can also be regarded as linear combinations of noise $\mathbf{z}_L - \mathbf{z}_H$ and HQ image latent representation \mathbf{z}_H . The SNR of \mathbf{z}_L is

$$\text{SNR}(\mathbf{z}_L) = \frac{\mathbb{E}[\mathbf{z}_H^2]}{\mathbb{E}[(\mathbf{z}_L - \mathbf{z}_H)^2]} \quad (4)$$

3.3.2. Average Optimal Mid-timestep

Given N LQ-HQ image latent representation pairs $\{(\mathbf{z}_L^{(i)}, \mathbf{z}_H^{(i)})\}, i \in \{1, \dots, N\}$ that are encoded by the VAE encoder in a dataset, we obtain an average optimal mid-timestep t^* by traversing all $t \in \{999, \dots, 1\}$ via:

$$t^* = \arg \min_t \frac{1}{N} \sum_i \left| \text{SNR}(\mathbf{z}_t^{(i)}) - \text{SNR}(\mathbf{z}_L^{(i)}) \right| \quad (5)$$

3.4. Architecture of OMGSR

The OMGSR framework in Fig. 2, is built on the GAN training [8], consisting of a generator and a discriminator.

3.5. Generator

Upon selecting an average optimal timestep t^* , we employ a classical DDPM-based generative model (e.g. SD2.1-base [29]). We fine-tune its VAE encoder and UNet via LoRA [12] to perform one-step denoising by injecting the LQ image latent representation at timestep t^* , and subsequently reconstruct the pixel-level image via the VAE decoder. This process is subsequently combined with GAN-based training to accomplish the Real-ISR task. Note that, within this framework, the DDPM-based generative model is regarded as the GAN generator.

3.5.1. Latent Representation Refinement (LRR) Loss

Although an average optimal t^* has been determined, we still aim to achieve sample-level refinement of the mapping from \mathbf{z}_L to \mathbf{z}_t through parameter fine-tuning during training. Specifically, we apply the LoRA injections to the VAE encoder \mathcal{E}_ϖ , to optimize the LoRA parameters ϖ . To enable this sample-wise approximation, we propose the Latent Representation Refinement (LRR) Loss:

$$\mathcal{L}_{\text{LRR}}(\mathbf{x}_L, \mathbf{x}_H, t^*) = \mathbb{E} \left[\|\mathbf{z}_L - \mathbf{z}_{t^*}\|_2^2 \right], \quad (6)$$

$$\mathbf{z}_L = \mathcal{E}_\varpi(\mathbf{x}_L), \mathbf{z}_{t^*} = \sqrt{\bar{\alpha}_{t^*}} \cdot \mathcal{E}(\mathbf{x}_H) + \sqrt{1 - \bar{\alpha}_{t^*}} \cdot \epsilon.$$

Note that we adopt the L2 loss for consistency with the pre-training objective, as the KL divergence is equivalent to an L2 loss in DDPM training [11]. Moreover, the L2 loss provides a more stable gradient signal during training.

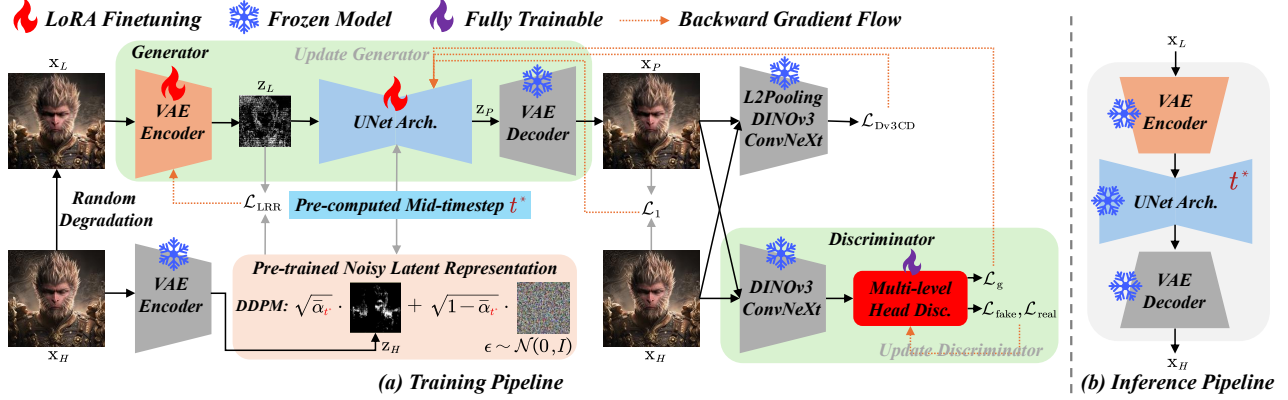


Figure 2. Illustration of our OMGSR-S training and inference pipelines. OMGSR-S achieves the fastest inference speed within SD-based Real-ISR models, as the input needs to pass through the VAE encoder, one-step prediction, and VAE decoder **only once**.

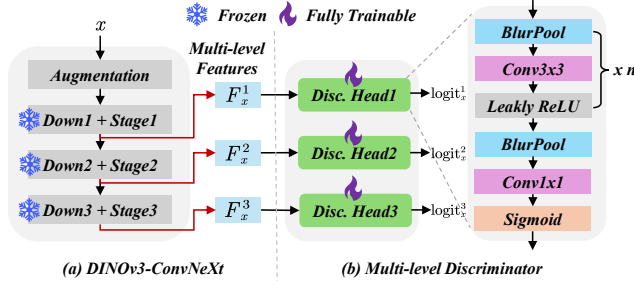


Figure 3. (a) **DINOv3-ConvNeXt** is used to extract multi-level features, which are fed into (b) **Multi-level Discriminator** to obtain the logits for discrimination. Note that **BlurPool** [57] is the low-pass filter used for anti-aliasing to prevent the artifacts.

3.5.2. One-step Prediction

After encoding via \mathcal{E}_ω , \mathbf{z}_L becomes more closely aligned with \mathbf{z}_{t^*} . We also apply LoRA fine-tuning to the denoising UNet ϵ_θ . The predicted noise is then used to perform a one-step denoising process ($t^* \rightarrow 0$), formulated as:

$$\mathbf{z}_P = \frac{\mathbf{z}_L - \sqrt{1 - \bar{\alpha}_{t^*}} \cdot \epsilon_\theta(\mathbf{z}_L, t^*, c)}{\sqrt{\bar{\alpha}_{t^*}}}. \quad (7)$$

Then, we obtain the predicted image: $\mathbf{x}_P = \mathcal{D}(\mathbf{z}_P)$.

3.6. Discriminator

3.6.1. DINOv3-ConvNeXt Features

The generator (*i.e.* DDPM-based generative model) possesses powerful image priors and demonstrates exceptional image generation capabilities. Unlike traditional GANs [8] that generate images from Gaussian noise, directly training a discriminator from scratch would lead to a significant imbalance, where the generator becomes too strong and the discriminator too weak.

Thus, we employ DINOv3-ConvNeXt [32], which also incorporates rich image priors. We consider it for feature

extraction for one main reason: its powerful extrapolation capability (achieved via RoPE [34]), which enables seamless adaptation to Real-ISR tasks at varying resolutions (up to 4K-resolution). This is particularly important as our proposed OMGSR is a framework designed to accommodate different DDPM-based generative models across varying resolutions (*e.g.* 1K-resolution).

Given the input image x , we adapt DINOv3-ConvNeXt (Dv3C) to extract multi-level features ($l = 1, 2, 3$):

$$\begin{aligned} \text{Dv3C}(x) &= \{F_x^l\}, F_x^0 = x, \\ F_x^l &= \text{Stage}_l(\text{Down}_l(F_x^{l-1})), \end{aligned} \quad (8)$$

where Down_l and Stage_l denote the l -th downsampling and feature extraction layers in DINOv3-ConvNeXt, respectively. The model comprises four main stages, enabling feature extraction at four distinct levels. The first three levels primarily contain detailed information, whereas the final level mainly encompasses global semantic information. Since \mathbf{z}_P in Eq. (7) is denoised from \mathbf{z}_L and already incorporates global semantic information but lacks detailed information, only the first three levels are utilized for feature extraction.

3.6.2. Multi-level Discriminator

We design the multi-level discriminator heads DiscHead_l , which take $\{F_x^l\}$, $l = 1, 2, 3$ as the input to predict the multi-level logits for discrimination, as illustrated in Fig. 3. We define the discrimination process as:

$$\begin{aligned} \text{Disc}(x) &= \{\text{logit}_x^l\}, \\ \text{logit}_x^l &= \text{Sigmoid}(\text{DiscHead}_l(F_x^l)). \end{aligned} \quad (9)$$

3.7. Generator Losses

3.7.1. DINOv3-ConvNeXt DISTs (Dv3CD) Loss

In GAN training [8], structural perception loss has been shown to play a critical role by preserving global structural

information of the image, while the GAN component focuses on refining local details. Most existing methods adopt LPIPS [58] as the perceptual loss. However, we note that LPIPS is built on a VGG [33] pre-trained on 224×224 images, which limits its effectiveness when training GANs at higher resolutions such as 512 or 1K, often leading to structural artifacts in the generated images.

We propose the DINOv3-ConvNeXt DISTs (Dv3CD) loss to address the resolution-mismatch problem. Following Eq. (8), we also utilize DINOv3-ConvNeXt and incorporate an $L2\text{Pooling}_l$ after each l -th stage to gather global structural information for structural perception. The main reason we use DINOv3-ConvNeXt is the same as in Sec. 3.6.1: its powerful extrapolation capability.

Given the input image x , we define the L2-pooling DINOv3-ConvNeXt (L2Dv3C) to extract the first three level L2-pooling features ($l = 1, 2, 3$):

$$\begin{aligned} L2Dv3C(x) &= \{L_x^l\}, L_x^0 = x, \\ L_x^l &= L2\text{Pooling}_l(\text{Stage}_l(\text{Down}_l(L_x^{l-1}))), \\ L2\text{Pooling}(\square) &= \sqrt{\text{Conv}2d(\square^2, w_h)}, \end{aligned} \quad (10)$$

where w_h is the 2D Hanning window filters [27].

Then we obtain the L2-pooling features of $\mathbf{x}_P, \mathbf{x}_H$ via $L2Dv3C(\mathbf{x}_P) = \{L_{\mathbf{x}_P}^l\}, L2Dv3C(\mathbf{x}_H) = \{L_{\mathbf{x}_H}^l\}$ in our OMGSR framework. We also include $L_{\mathbf{x}_P}^0 = \mathbf{x}_P, L_{\mathbf{x}_H}^0 = \mathbf{x}_H$ for calculation. Then Dv3CD loss is calculated via the DISTs [6] ($l = 0, 1, 2, 3$):

$$\begin{aligned} \mathcal{L}_{Dv3CD}(\mathbf{x}_P, \mathbf{x}_H) &= \text{DISTs}(\{L_{\mathbf{x}_P}^l\}, \{L_{\mathbf{x}_H}^l\}) \\ &= 1 - \frac{1}{\alpha} \sum_{l=0}^3 \mathbb{E} \left[\frac{2\mu_{L_{\mathbf{x}_P}^l} \mu_{L_{\mathbf{x}_H}^l}}{\mu_{L_{\mathbf{x}_P}^l}^2 + \mu_{L_{\mathbf{x}_H}^l}^2} + \frac{2\sigma_{L_{\mathbf{x}_P}^l, L_{\mathbf{x}_H}^l}}{\sigma_{L_{\mathbf{x}_P}^l}^2 + \sigma_{L_{\mathbf{x}_H}^l}^2} \right], \end{aligned} \quad (11)$$

where $\mu_{\square}, \sigma_{\square}$, and $\sigma_{\square, \square}$ denote the mean, variance, and covariance computed across the 2D spatial dimensions of the feature maps, respectively. The coefficient α is defined as $\alpha = 2 \sum_{l=0}^3 C(L_{\mathbf{x}_H}^l)$, where the function $C(\square)$ denotes the number of channels.

3.7.2. Generator GAN Loss

We directly employ the standard GAN loss, as the GAN training in Real-ISR follows an LQ→HQ mapping rather than a Noise→HQ paradigm, making the learning task relatively easy and stable. We obtain the logits of \mathbf{x}_P via $\text{Disc}(\mathbf{x}_P) = \{\text{logit}_{\mathbf{x}_P}^l\}$. Then the generator GAN loss is:

$$\mathcal{L}_g(\mathbf{x}_P) = \sum_{l=1}^3 \mathbb{E} \left[\text{BCE}(\text{logit}_{\mathbf{x}_P}^l, \text{label}_{\text{real}}) \right], \quad (12)$$

where $\text{label}_{\text{real}}$ is the soft label, and set to 0.8. The function BCE denotes the binary cross-entropy.

3.7.3. Complete Generator Loss

For the generator, a structural perception loss is required to preserve the overall structure, while the generator GAN loss ensures the fine details. We also employ an L1 loss \mathcal{L}_1 for pixel-level constraints. We only update the parameters of the VAE encoder and UNet. The complete generator loss is

$$\begin{aligned} \mathcal{L}_G(\mathbf{x}_L, \mathbf{x}_P, \mathbf{x}_H) &= \lambda_1 \mathcal{L}_{\text{LRR}}(\mathbf{x}_L, \mathbf{x}_H, t^*) + \lambda_2 \mathcal{L}_g(\mathbf{x}_P) \\ &+ \lambda_3 \mathcal{L}_{Dv3CD}(\mathbf{x}_P, \mathbf{x}_H) + \lambda_4 \mathcal{L}_1(\mathbf{x}_P, \mathbf{x}_H). \end{aligned} \quad (13)$$

3.8. Discriminator Losses

3.8.1. Discriminator GAN Loss

For discriminator training, we only update its parameters, aiming to discriminate between fake and real images. We obtain the logits of $\mathbf{x}_{\hat{P}} = \text{Detach}(\mathbf{x}_P), \mathbf{x}_H$ via $\text{Disc}(\mathbf{x}_{\hat{P}}) = \{\text{logit}_{\mathbf{x}_{\hat{P}}}^l\}, \text{Disc}(\mathbf{x}_H) = \{\text{logit}_{\mathbf{x}_H}^l\}$. Then the discriminator GAN loss is:

$$\begin{aligned} \mathcal{L}_{\text{fake}}(\mathbf{x}_{\hat{P}}) &= \sum_{l=1}^3 \mathbb{E} \left[\text{BCE}(\text{logit}_{\mathbf{x}_{\hat{P}}}^l, \text{label}_{\text{fake}}) \right], \\ \mathcal{L}_{\text{real}}(\mathbf{x}_H) &= \sum_{l=1}^3 \mathbb{E} \left[\text{BCE}(\text{logit}_{\mathbf{x}_H}^l, \text{label}_{\text{real}}) \right], \end{aligned} \quad (14)$$

where $\text{label}_{\text{fake}}$ is set to 0.

3.8.2. Complete Discriminator Loss

The complete discriminator loss consists of $\mathcal{L}_{\text{fake}}$ and $\mathcal{L}_{\text{real}}$:

$$\mathcal{L}_D(\mathbf{x}_{\hat{P}}, \mathbf{x}_H) = \lambda_2 (\mathcal{L}_{\text{fake}}(\mathbf{x}_{\hat{P}}) + \mathcal{L}_{\text{real}}(\mathbf{x}_H)). \quad (15)$$

4. Experiments

4.1. Experimental Settings

4.1.1. Training Settings.

We follow SeeSR [47], utilizing LSDIR [19] dataset and the first 10,000 face images from FFHQ [14] for the $\times 4$ SR task. LQ-HQ image pairs are synthesized via the standard Real-ESRGAN [41] degradation pipeline. Within the OMGSR framework, we adapt the SD2.1 base as the foundation model to instantiate OMGSR-S. For LoRA injection, we set the VAE LoRA rank to 16 and the UNet LoRA rank to 32. We employ the AdamW [22] optimizer with a learning rate of 5×10^{-5} , a batch size of 1, and 4 gradient steps, training on four RTX 4090 GPUs for 5100 steps. We set $\lambda_1 = 5, \lambda_2 = 0.5, \lambda_3 = 5, \lambda_4 = 0.5$ in Eq. (13).

4.1.2. Test Dataset

Since OMGSR focuses on Real-ISR tasks, we test it on four classic datasets: RealSR [4], DrealSR [45], RealLQ250 [1], and RealLR200 [47]. Among these, RealSR contains 100 images of size 128×128 , and DrealSR includes 93 images of the same size. RealLQ250 comprises 250 images

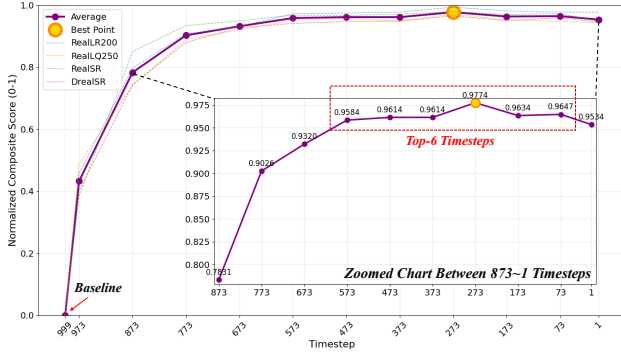


Figure 4. Ablation Study of OMGRS-S with different timesteps. We set the timestep 273 as the baseline, with intervals of 100. Note that we conduct experiments on OMGRS-S **without** the proposed LRR Loss to avoid any impact on the latent representation. We report a normalized score based on 9 metrics across four datasets. The details are in the **supplementary materials**.

with dimensions 256×256 , while RealLR200 consists of 200 images with varying resolutions. For RealLQ250 and RealLR200, tiled diffusion is required during testing. We conduct all experiments on the $\times 4$ Real-ISR task.

4.1.3. Metrics

Traditional reference metrics like PSNR, SSIM [43] struggle to reflect the real visual effects of the generated images [2, 13, 52]. Thus, we use model-based reference metrics: LPIPS [58] and FID [9]; non-reference metrics: CLIPQA [37], CLIPQA+ [37], NIMA [36], NIQE [24], LIQE [59], MUSIQ [15], and MANIQA [48]. These metrics reflect the image quality in multiple ways. In this paper, we use the PyIQA [5] tool to evaluate these metrics.

4.2. Ablation Study

4.2.1. Ablation Study on Timestep

We ablate the different timesteps using OMGRS-S **without** LRR loss. Note that we do not include LRR loss to avoid its effect on latent representation. The baseline timestep is 273 calculated from Eq. (5). Performance is evaluated at 100-timestep intervals, with results aggregated into a composite score (0–1) using normalized metrics across four datasets.

As shown in Fig. 4, injecting the LQ image latent \mathbf{z}_L in early timesteps (999–673) severely degrades performance, whereas mid-to-late injections (573–173) yield high and stable results. The peak occurs at timestep 273, aligning with the theoretically derived value in Eq. (5). This confirms that our SNR-based method effectively guides the selection of timesteps in DDPM-based Real-ISR.

4.2.2. Ablation Study on Architecture

To further validate Eq. (5), we conduct an ablation study on OSediff [46] with $t = 999$ (original paper settings) vs.

Table 1. Ablation study of OSediff with $t = 999$ vs. $t = 273$.

Dataset	Model	CLIPQA \uparrow	CLIPQA+ \uparrow	NIMA \uparrow	NIQE \downarrow	LIQE \uparrow	MUSIQ \uparrow	MANIQA \uparrow
RealSR	999	0.6582	0.6798	4.7581	5.4996	3.7536	67.5307	0.6223
	273	0.6589	0.6853	4.7760	5.4132	3.8060	68.0663	0.6400
DrealSR	999	0.6937	0.6864	4.6248	6.3676	3.7991	64.1535	0.5917
	273	0.6857	0.6808	4.6136	5.8439	3.7600	64.7893	0.6072
RealLR250	999	0.7103	0.7131	5.1855	4.0279	3.8323	70.2660	0.6019
	273	0.7353	0.7349	5.2604	3.8477	4.0427	71.5111	0.6251
RealLR200	999	0.7077	0.7154	5.3150	4.0738	3.9358	69.4883	0.6194
	273	0.7281	0.7379	5.3817	3.9197	4.1321	70.9423	0.6421

Table 2. Ablation Study of \mathcal{L}_{LRR} . The baseline denotes OMGRS-S without the \mathcal{L}_{LRR} . We define $\mathcal{L}_{TOHQ} = \mathbb{E}[\|\mathbf{z}_L - \mathbf{z}_H\|_2^2]$.

Dataset	Method	CLIPQA \uparrow	CLIPQA+ \uparrow	NIMA \uparrow	NIQE \downarrow	LIQE \uparrow	MUSIQ \uparrow	MANIQA \uparrow
RealSR	baseline	0.6352	0.6785	4.9030	5.6487	4.1373	68.5648	0.6756
	w/ \mathcal{L}_{TOHQ}	0.6607	0.7025	5.0079	5.5170	4.3073	69.4674	0.6701
	w/ \mathcal{L}_{LRR}	0.6709	0.7143	5.0025	5.1893	4.3509	69.9406	0.6753
DrealSR	baseline	0.6552	0.6650	4.7416	6.5184	3.9885	65.3381	0.6259
	w/ \mathcal{L}_{TOHQ}	0.6993	0.6962	4.7910	6.0305	4.2286	66.2147	0.6276
	w/ \mathcal{L}_{LRR}	0.6958	0.7053	4.8008	5.7720	4.2775	66.6773	0.6354
RealLR250	baseline	0.6976	0.7065	5.1490	4.0240	3.9954	69.8671	0.6302
	w/ \mathcal{L}_{TOHQ}	0.7176	0.7217	5.1664	3.9883	4.1499	70.2378	0.6287
	w/ \mathcal{L}_{LRR}	0.7318	0.7352	5.2356	3.8771	4.2546	71.0128	0.6385
RealLR200	baseline	0.7016	0.7211	5.3617	4.0731	4.1901	69.8960	0.6571
	w/ \mathcal{L}_{TOHQ}	0.7170	0.7332	5.3649	4.0693	4.2865	70.4493	0.6582
	w/ \mathcal{L}_{LRR}	0.7297	0.7456	5.3928	3.9628	4.3806	71.0941	0.6646

$t = 273$ (our paper settings). Note that the degradation configuration of OSediff is the same as that of OMGRS-S, thus 273 is also available to OSediff. We keep all basic OSediff settings unchanged and train both models for 17,000 steps with a batch size of 1 and a gradient step size of 4 on four NVIDIA RTX 4090 GPUs.

As shown in Tab. 1, OSediff ($t = 273$) significantly outperforms OSediff ($t = 999$) across all datasets and metrics. Most metrics (*e.g.* MANIQA, MUSIQ) of OSediff ($t = 273$) also surpass those reported in Tab. 3. These results further confirm our analysis of mid-timestep and the effectiveness of our SNR-based method in Eq. (5).

4.2.3. Ablation study on LRR Loss

To evaluate the effectiveness of the proposed \mathcal{L}_{LRR} , we ablate OMGRS-S under three settings: (1) **without** \mathcal{L}_{LRR} (baseline), (2) **with** \mathcal{L}_{LRR} , and (3) **with** \mathcal{L}_{TOHQ} , a variant that approximates the HQ image latent \mathbf{z}_H instead of the noisy pre-trained latent \mathbf{z}_{t^*} *i.e.* $\mathcal{L}_{TOHQ} = \mathbb{E}[\|\mathbf{z}_L - \mathbf{z}_H\|_2^2]$.

Results in Tab. 2 show two key findings: **First**, both \mathcal{L}_{LRR} and \mathcal{L}_{TOHQ} bring consistent and significant gains over the baseline across all datasets and metrics, confirming that guiding \mathbf{z}_L toward either \mathbf{z}_H or \mathbf{z}_{t^*} is beneficial. **Second**, \mathcal{L}_{LRR} outperforms \mathcal{L}_{TOHQ} on nearly all metrics, indicating that aligning with the pre-trained noisy latent \mathbf{z}_{t^*} better activates the generative prior by adhering to the model’s inherent training rules.

4.2.4. Ablation Study on Dv3CD Loss

We ablate two structural perception losses: \mathcal{L}_{LPIPS} and \mathcal{L}_{Dv3CD} on OMGRS-S. As shown in Tab. 4, \mathcal{L}_{Dv3CD} achieves better results in 23 out of 28 metrics across four datasets. Although \mathcal{L}_{LPIPS} yields slightly better NIQE on

Table 3. Quantitative comparisons ($\times 4$) with state-of-the-art multi-step and one-step models on four real-world benchmark datasets. The best and second-best results of each metric are highlighted in bold and underlined, respectively. "-s" denotes the number of diffusion steps.

Datasets	Metrics	RealESRGAN [41]	StableSR [38] -s200	SeeSR [47] -s50	DiffBIR [20] -s50	ResShift [53] -s15	SinSR [42] -s1	OSEDiff [46] -s1	InvSR [54] -s1	PiSA-SR [35] -s1	OMGSR-S -s1
RealSR	LPIPS↓	0.2710	0.2604	0.3007	0.3470	0.3159	0.3210	0.2921	0.2871	<u>0.2672</u>	0.3009
	FID↓	135.15	132.09	125.51	134.59	149.65	136.78	123.50	138.85	124.19	<u>124.05</u>
	CLIQQA↑	0.4490	0.5426	0.6699	0.6960	0.5505	0.6156	0.6693	0.6785	0.6699	0.6709
	CLIQQA+↑	0.5841	0.6150	0.6909	<u>0.6989</u>	0.5451	0.5370	0.6964	0.6880	0.6957	0.7143
	NIMA↑	4.6551	4.6767	4.9191	4.9159	4.7554	4.6643	4.8951	5.0946	4.8953	<u>5.0025</u>
	NIQE↓	5.7960	6.6231	<u>5.3984</u>	5.4992	6.8833	6.2998	5.6474	5.6222	5.5057	5.1893
	LIQE↑	3.3571	3.2578	4.1354	4.0261	3.1859	3.1466	4.0690	4.0392	<u>4.0989</u>	4.3509
	MUSIQ↑	60.3657	61.8058	69.8165	68.3462	60.2181	60.4204	69.0896	68.5372	70.1492	<u>69.9406</u>
	MANIQA↑	0.5492	0.5952	0.6445	0.6540	0.5388	0.5391	0.6331	<u>0.6628</u>	0.6552	0.6753
DrealSR	LPIPS↓	<u>0.2819</u>	0.2698	0.3174	0.4520	0.3526	0.3674	0.2968	0.3538	0.2960	0.3267
	FID↓	147.80	151.27	147.53	177.06	176.70	171.88	<u>135.29</u>	171.40	130.43	142.44
	CLIQQA↑	0.4517	0.4907	0.6913	0.6859	0.5410	0.6348	0.6963	0.7132	<u>0.6974</u>	0.6958
	CLIQQA+↑	0.5544	0.5347	0.6794	0.6828	0.5157	0.5400	0.6825	<u>0.6832</u>	0.6920	0.7053
	NIMA↑	4.3261	4.2136	4.6945	4.7847	4.4405	4.4639	4.6766	4.8566	4.6250	<u>4.8008</u>
	NIQE↓	6.6927	7.5488	6.4136	6.2409	7.8693	7.1422	6.4904	<u>5.9177</u>	6.1759	5.7720
	LIQE↑	2.9259	2.4349	<u>4.1268</u>	3.8930	2.7968	3.0514	3.9371	4.0557	4.0440	4.2775
	MUSIQ↑	54.2721	51.3635	65.0935	65.6585	52.3726	54.9825	64.6537	65.9956	<u>66.1094</u>	66.6773
	MANIQA↑	0.4899	0.4969	0.6043	0.6279	0.4750	0.4855	0.5895	<u>0.6302</u>	0.6146	0.6753
RealLQ250	CLIQQA↑	0.5434	0.5150	0.7132	<u>0.7255</u>	0.4734	0.6998	0.6995	0.6628	0.7095	0.7318
	CLIQQA+↑	0.6117	0.5811	0.7142	<u>0.7213</u>	0.4642	0.5919	0.7017	0.6722	0.7160	0.7352
	NIMA↑	5.2554	5.0700	5.3863	5.4922	5.0243	5.1938	5.2364	<u>5.4401</u>	5.2429	5.2356
	NIQE↓	4.1292	4.6345	3.9832	3.5608	4.8476	5.7974	3.9127	4.4098	<u>3.8751</u>	3.8771
	LIQE↑	3.3410	2.7533	<u>4.1336</u>	4.0874	2.4609	3.2465	3.8610	3.7113	3.9813	4.2546
	MUSIQ↑	62.5169	57.1341	71.1218	70.3687	57.7724	63.8548	69.6786	65.8212	<u>71.0710</u>	71.0128
	MANIQA↑	0.5288	0.5203	0.6204	<u>0.6232</u>	0.4657	0.5178	0.5928	0.5914	0.6157	0.6385
	RealLQ200	CLIQQA↑	0.5409	0.5731	0.6959	<u>0.7222</u>	0.4942	0.6615	0.7008	0.6830	0.7125
CLIQQA+↑		0.6222	0.6360	0.7171	0.7241	0.5094	0.5888	0.7136	0.7111	<u>0.7292</u>	0.7456
NIMA↑		5.1866	5.2607	5.4154	<u>5.4648</u>	5.0419	5.1763	5.3530	5.5045	5.3920	5.3928
NIQE↓		4.1796	4.3515	3.9996	3.7803	4.8432	5.3042	<u>3.9268</u>	3.9936	3.9991	3.9628
LIQE↑		3.4836	3.4319	<u>4.1806</u>	4.0541	2.6938	3.2175	3.9967	4.0778	4.1690	4.3806
MUSIQ↑		62.9605	63.3346	<u>70.2502</u>	68.7120	57.4580	61.3634	69.5654	68.9061	<u>70.8834</u>	71.0941
MANIQA↑		0.5553	0.5749	0.6360	0.6385	0.4925	0.5343	0.6143	0.6481	<u>0.6418</u>	0.6646

Table 4. Ablation study of OMGSR-S with \mathcal{L}_{LPIPS} vs. \mathcal{L}_{Dv3CD} .

Dataset	Loss	CLIQQA↑	CLIQQA+↑	NIMA↑	NIQE↓	LIQE↑	MUSIQ↑	MANIQA↑
RealSR	\mathcal{L}_{LPIPS}	0.6422	0.7052	4.8855	5.2712	4.2258	69.6518	0.6776
	\mathcal{L}_{Dv3CD}	0.6709	0.7143	5.0025	5.1893	4.3509	69.9406	0.6753
DrealSR	\mathcal{L}_{LPIPS}	0.6732	0.6867	4.6917	5.9989	4.1462	65.9111	0.6353
	\mathcal{L}_{Dv3CD}	0.6958	0.7053	4.8008	5.7720	4.2775	66.6773	0.6354
RealLR250	\mathcal{L}_{LPIPS}	0.7179	0.7276	5.2164	3.7442	4.2085	71.3788	0.6415
	\mathcal{L}_{Dv3CD}	0.7318	0.7352	5.2356	3.8771	4.2546	71.0128	0.6385
RealLR200	\mathcal{L}_{LPIPS}	0.7121	0.7354	5.3271	3.9039	4.2888	70.8682	0.6610
	\mathcal{L}_{Dv3CD}	0.7297	0.7456	5.3928	3.9628	4.3806	71.0941	0.6646

two datasets, \mathcal{L}_{Dv3CD} shows a clear overall advantage.

Visually, as shown in Fig. 5, \mathcal{L}_{LPIPS} leads to noticeable artifacts, while \mathcal{L}_{Dv3CD} produces artifact-free results. This stems from the resolution limit of \mathcal{L}_{LPIPS} , which is designed for inputs up to 224×224 , which is far smaller than the 512×512 images typically used in Real-ISR. In contrast, \mathcal{L}_{Dv3CD} is built on DINOv3-ConvNeXt, which natively supports higher resolutions such as 512 and beyond, enabling more stable and faithful image reconstruction.

4.3. Comparison Results

We compare OMGSR-S with the state-of-the-art SD-based models under the same foundation model size, including multi-step models (StableSR [38], SeeSR [47], DiffBIR [20], ResShift [53]), and one-step models (OSEDiff [38], SinSR [42], InvSR [54], PiSA-SR [35]). We also include RealESRGAN [41] as the baseline for reference.



Figure 5. A artifact case in OMGSR-S with \mathcal{L}_{LPIPS} vs. \mathcal{L}_{Dv3CD} .

Here, we evaluate all the models on an RTX 4090.

4.3.1. Quantitative Comparisons

As summarized in Tab. 3, our proposed OMGSR-S demonstrates highly competitive performance across all datasets and evaluation metrics. The quantitative results show that our method consistently achieves excellent performance, ranking first or second in most quality assessments. This consistent performance across diverse real-world benchmarks validates the effectiveness of our approach in handling various degradation patterns present in real images. Considering that we employ \mathcal{L}_{Dv3CD} Loss instead of \mathcal{L}_{LPIPS} , our method typically yields lower LPIPS metrics compared to models optimized with \mathcal{L}_{LPIPS} , such as PiSA-SR and OSEDiff.

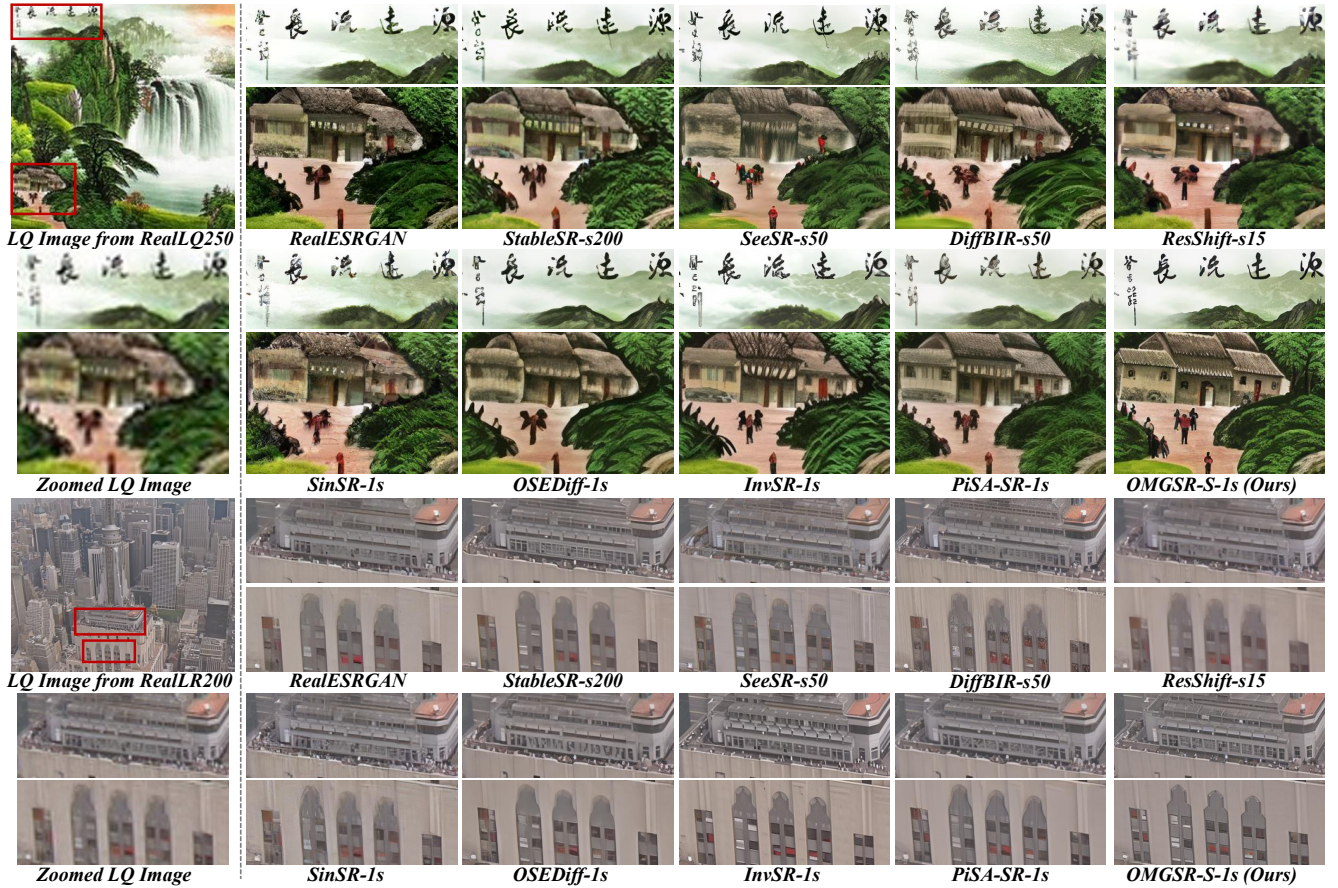


Figure 6. Qualitative comparisons with state-of-the-art multi-step and one-step models on two complex cases from ReallQ250 and ReallR200. Please zoom in for a detailed visualization. More qualitative comparisons can be found in the **supplementary materials**.

4.3.2. Qualitative Comparisons

Visual comparisons are presented in Fig. 6. **First case:** In the first row, OSediff and OMGSR-S produce relatively higher textual quality compared to others, while OMGSR-S exhibits the best overall text clarity and structure. In the second row, RealESRGAN, SeeSR, ResShift, and SinSR struggle to generate the thatched cottage in the painting, whereas DiffBIR and OSediff roughly construct the basic form of the cottage. DiffBIR, InvSR, and PiSA-SR can generate basic thatched cottages. At the same time, our proposed OMGSR-S produces the best structural integrity and clarity in the generated cottage. **Second case:** In the first row, StableSR, InvSR, and OMGSR reconstruct complex scenes more effectively than other models, with OMGSR-S demonstrating superior clarity and detail. In the second row, InvSR and OMGSR-S produce more plausible scene reconstructions, while OMGSR-S achieves even greater clarity. Through these two complex scene cases, it can be observed that OMGSR-S excels in preserving finer details and structural coherence under challenging reconstruction scenarios.

5. Conclusion

Summary. This work presents OMGSR, a universal GAN-based framework that employs a DDPM-based generative model as the generator and a DINOv3-ConvNeXt model with a multi-level discriminator as the discriminator. To effectively leverage generative priors, we first examine the role of mid-timestep injection in DDPM-based models and propose an SNR-based method to pre-compute an average optimal timestep. Furthermore, we introduce the Latent Representation Refinement (LRR) loss to enhance the VAE encoder by minimizing the latent representation gap. In addition, we design the DINOv3-ConvNeXt DISTS (Dv3CD) loss to improve structural perception, addressing the resolution mismatch between the model’s supported input and the RealISR’s training input. Within the OMGSR framework, we develop OMGSR-S (SD2.1-base), which achieves state-of-the-art performance across multiple metrics on four real-world datasets. **Note.** The OMGSR framework is also compatible with flow matching [21] models, such as FLUX.1-dev [17]. We also provide an analysis of flow matching within OMGSR and develop OMGSR-F. Further details can be found in the **supplementary materials**.

References

- [1] Yuang Ai, Xiaoqiang Zhou, Huaibo Huang, Xiaotian Han, Zhengyu Chen, Quanzeng You, and Hongxia Yang. Dreamclear: High-capacity real-world image restoration with privacy-safe dataset curation. *Advances in Neural Information Processing Systems*, 37:55443–55469, 2024. 5
- [2] Yochai Blau and Tomer Michaeli. The perception-distortion tradeoff. In *Proceedings of the IEEE conference on computer vision and pattern recognition*, pages 6228–6237, 2018. 6
- [3] Jianrui Cai, Hui Zeng, Hongwei Yong, Zisheng Cao, and Lei Zhang. Toward real-world single image super-resolution: A new benchmark and a new model. In *Proceedings of the IEEE/CVF international conference on computer vision*, pages 3086–3095, 2019. 1
- [4] Jianrui Cai, Hui Zeng, Hongwei Yong, Zisheng Cao, and Lei Zhang. Toward real-world single image super-resolution: A new benchmark and a new model. In *Proceedings of the IEEE/CVF international conference on computer vision*, pages 3086–3095, 2019. 5
- [5] Chaofeng Chen and Jiadi Mo. IQA-PyTorch: Pytorch toolbox for image quality assessment. [Online]. Available: <https://github.com/chaofengc/IQA-PyTorch>, 2022. 6
- [6] Keyan Ding, Kede Ma, Shiqi Wang, and Eero P Simoncelli. Image quality assessment: Unifying structure and texture similarity. *IEEE transactions on pattern analysis and machine intelligence*, 44(5):2567–2581, 2020. 5
- [7] Chao Dong, Chen Change Loy, Kaiming He, and Xiaoou Tang. Image super-resolution using deep convolutional networks. *IEEE transactions on pattern analysis and machine intelligence*, 38(2):295–307, 2015. 1
- [8] Ian J Goodfellow, Jean Pouget-Abadie, Mehdi Mirza, Bing Xu, David Warde-Farley, Sherjil Ozair, Aaron Courville, and Yoshua Bengio. Generative adversarial nets. *Advances in neural information processing systems*, 27, 2014. 3, 4
- [9] Martin Heusel, Hubert Ramsauer, Thomas Unterthiner, Bernhard Nessler, and Sepp Hochreiter. Gans trained by a two time-scale update rule converge to a local nash equilibrium. *Advances in neural information processing systems*, 30, 2017. 6
- [10] Geoffrey Hinton, Oriol Vinyals, and Jeff Dean. Distilling the knowledge in a neural network. *arXiv preprint arXiv:1503.02531*, 2015. 2
- [11] Jonathan Ho, Ajay Jain, and Pieter Abbeel. Denoising diffusion probabilistic models. *Advances in neural information processing systems*, 33:6840–6851, 2020. 3
- [12] Edward J Hu, Yelong Shen, Phillip Wallis, Zeyuan Allen-Zhu, Yuanzhi Li, Shean Wang, Lu Wang, and Weizhu Chen. LoRA: Low-rank adaptation of large language models. In *International Conference on Learning Representations*, 2022. 1, 3
- [13] Gu Jinjin, Cai Haoming, Chen Haoyu, Ye Xiaoxing, Jimmy S Ren, and Dong Chao. Pipal: a large-scale image quality assessment dataset for perceptual image restoration. In *European conference on computer vision*, pages 633–651. Springer, 2020. 6
- [14] Tero Karras, Samuli Laine, and Timo Aila. A style-based generator architecture for generative adversarial networks. In *Proceedings of the IEEE/CVF conference on computer vision and pattern recognition*, pages 4401–4410, 2019. 5
- [15] Junjie Ke, Qifei Wang, Yilin Wang, Peyman Milanfar, and Feng Yang. Musiq: Multi-scale image quality transformer. In *Proceedings of the IEEE/CVF international conference on computer vision*, pages 5148–5157, 2021. 6
- [16] Jaeha Kim, Junghun Oh, and Kyoung Mu Lee. Exploiting diffusion prior for task-driven image restoration. In *Proceedings of the IEEE/CVF International Conference on Computer Vision*, pages 10151–10161, 2025. 1
- [17] Black Forest Labs. Flux. <https://github.com/black-forest-labs/flux>, 2024. 8
- [18] Christian Ledig, Lucas Theis, Ferenc Huszár, Jose Caballero, Andrew Cunningham, Alejandro Acosta, Andrew Aitken, Alykhan Tejani, Johannes Totz, Zehan Wang, et al. Photo-realistic single image super-resolution using a generative adversarial network. In *Proceedings of the IEEE conference on computer vision and pattern recognition*, pages 4681–4690, 2017. 1
- [19] Yawei Li, Kai Zhang, Jingyun Liang, Jiezhang Cao, Ce Liu, Rui Gong, Yulun Zhang, Hao Tang, Yun Liu, Denis Deman-dolz, et al. Lsdir: A large scale dataset for image restoration. In *Proceedings of the IEEE/CVF Conference on Computer Vision and Pattern Recognition*, pages 1775–1787, 2023. 5
- [20] Xinqi Lin, Jingwen He, Ziyang Chen, Zhaoyang Lyu, Bo Dai, Fanghua Yu, Yu Qiao, Wanli Ouyang, and Chao Dong. Diff-bir: Toward blind image restoration with generative diffusion prior. In *European conference on computer vision*, pages 430–448. Springer, 2024. 1, 2, 7
- [21] Yaron Lipman, Ricky T. Q. Chen, Heli Ben-Hamu, Maximilian Nickel, and Matthew Le. Flow matching for generative modeling. In *The Eleventh International Conference on Learning Representations*, 2023. 8
- [22] Ilya Loshchilov and Frank Hutter. Decoupled weight decay regularization. In *International Conference on Learning Representations*, 2019. 5
- [23] Ziwei Luo, Fredrik Gustafsson, Zheng Zhao, Jens Sjölund, and Thomas Schön. Taming diffusion models for image restoration: a review. *Philosophical Transactions A*, 383(2299):20240358, 2025. 1
- [24] Anish Mittal, Rajiv Soundararajan, and Alan C Bovik. Making a “completely blind” image quality analyzer. *IEEE Signal processing letters*, 20(3):209–212, 2012. 6
- [25] Brian B Moser, Arundhati S Shanbhag, Federico Raue, Stanislav Frolov, Sebastian Palacio, and Andreas Dengel. Diffusion models, image super-resolution, and everything: A survey. *IEEE Transactions on Neural Networks and Learning Systems*, 2024. 1
- [26] Aamir Mustafa, Aliaksei Mikhailiuk, Dan Andrei Iliescu, Varun Babbar, and Rafał K Mantiuk. Training a task-specific image reconstruction loss. In *Proceedings of the IEEE/CVF winter conference on applications of computer vision*, pages 2319–2328, 2022. 2
- [27] Nicolas Pielawski and Carolina Wählby. Introducing hann windows for reducing edge-effects in patch-based image segmentation. *PloS one*, 15(3):e0229839, 2020. 5

- [28] Haoyu Ren, Amin Kheradmand, Mostafa El-Khamy, Shuangquan Wang, Dongwoon Bai, and Jungwon Lee. Real-world super-resolution using generative adversarial networks. In *Proceedings of the IEEE/CVF Conference on Computer Vision and Pattern Recognition Workshops*, pages 436–437, 2020. 1
- [29] Robin Rombach, Andreas Blattmann, Dominik Lorenz, Patrick Esser, and Björn Ommer. High-resolution image synthesis with latent diffusion models. In *Proceedings of the IEEE/CVF conference on computer vision and pattern recognition*, pages 10684–10695, 2022. 1, 2, 3
- [30] Olaf Ronneberger, Philipp Fischer, and Thomas Brox. U-net: Convolutional networks for biomedical image segmentation. In *International Conference on Medical image computing and computer-assisted intervention*, pages 234–241. Springer, 2015. 2, 3
- [31] Wenzhe Shi, Jose Caballero, Ferenc Huszár, Johannes Totz, Andrew P Aitken, Rob Bishop, Daniel Rueckert, and Zehan Wang. Real-time single image and video super-resolution using an efficient sub-pixel convolutional neural network. In *Proceedings of the IEEE conference on computer vision and pattern recognition*, pages 1874–1883, 2016. 1
- [32] Oriane Siméoni, Huy V Vo, Maximilian Seitzer, Federico Baldassarre, Maxime Oquab, Cijo Jose, Vasil Khalidov, Marc Szafraniec, Seungeun Yi, Michaël Ramamonjisoa, et al. Dinov3. *arXiv preprint arXiv:2508.10104*, 2025. 4
- [33] Karen Simonyan and Andrew Zisserman. Very deep convolutional networks for large-scale image recognition. *arXiv preprint arXiv:1409.1556*, 2014. 5
- [34] Jianlin Su, Murtadha Ahmed, Yu Lu, Shengfeng Pan, Wen Bo, and Yunfeng Liu. Roformer: Enhanced transformer with rotary position embedding. *Neurocomputing*, 568:127063, 2024. 4
- [35] Lingchen Sun, Rongyuan Wu, Zhiyuan Ma, Shuaizheng Liu, Qiaosi Yi, and Lei Zhang. Pixel-level and semantic-level adjustable super-resolution: A dual-lora approach. In *Proceedings of the Computer Vision and Pattern Recognition Conference*, pages 2333–2343, 2025. 2, 3, 7
- [36] Hossein Talebi and Peyman Milanfar. Nima: Neural image assessment. *IEEE transactions on image processing*, 27(8):3998–4011, 2018. 6
- [37] Jianyi Wang, Kelvin CK Chan, and Chen Change Loy. Exploring clip for assessing the look and feel of images. In *Proceedings of the AAAI conference on artificial intelligence*, pages 2555–2563, 2023. 6
- [38] Jianyi Wang, Zongsheng Yue, Shangchen Zhou, Kelvin CK Chan, and Chen Change Loy. Exploiting diffusion prior for real-world image super-resolution. *International Journal of Computer Vision*, 132(12):5929–5949, 2024. 1, 2, 7
- [39] Jianyi Wang, Zongsheng Yue, Shangchen Zhou, Kelvin CK Chan, and Chen Change Loy. Exploiting diffusion prior for real-world image super-resolution. *International Journal of Computer Vision*, 132(12):5929–5949, 2024. 1
- [40] Xintao Wang, Yu Li, Honglun Zhang, and Ying Shan. Towards real-world blind face restoration with generative facial prior. In *Proceedings of the IEEE/CVF conference on computer vision and pattern recognition*, pages 9168–9178, 2021. 1
- [41] Xintao Wang, Liangbin Xie, Chao Dong, and Ying Shan. Real-esrgan: Training real-world blind super-resolution with pure synthetic data. In *Proceedings of the IEEE/CVF international conference on computer vision*, pages 1905–1914, 2021. 1, 5, 7
- [42] Yufei Wang, Wenhan Yang, Xinyuan Chen, Yaohui Wang, Lanqing Guo, Lap-Pui Chau, Ziwei Liu, Yu Qiao, Alex C Kot, and Bihan Wen. Sinsr: diffusion-based image super-resolution in a single step. In *Proceedings of the IEEE/CVF conference on computer vision and pattern recognition*, pages 25796–25805, 2024. 2, 7
- [43] Zhou Wang, Alan C Bovik, Hamid R Sheikh, and Eero P Simoncelli. Image quality assessment: from error visibility to structural similarity. *IEEE transactions on image processing*, 13(4):600–612, 2004. 6
- [44] Zhihao Wang, Jian Chen, and Steven CH Hoi. Deep learning for image super-resolution: A survey. *IEEE transactions on pattern analysis and machine intelligence*, 43(10):3365–3387, 2020. 1
- [45] Pengxu Wei, Ziwei Xie, Hannan Lu, Zongyuan Zhan, Qixiang Ye, Wangmeng Zuo, and Liang Lin. Component divide-and-conquer for real-world image super-resolution. In *European conference on computer vision*, pages 101–117. Springer, 2020. 5
- [46] Rongyuan Wu, Lingchen Sun, Zhiyuan Ma, and Lei Zhang. One-step effective diffusion network for real-world image super-resolution. *Advances in Neural Information Processing Systems*, 37:92529–92553, 2024. 2, 3, 6, 7
- [47] Rongyuan Wu, Tao Yang, Lingchen Sun, Zhengqiang Zhang, Shuai Li, and Lei Zhang. Seesr: Towards semantics-aware real-world image super-resolution. In *Proceedings of the IEEE/CVF conference on computer vision and pattern recognition*, pages 25456–25467, 2024. 2, 5, 7
- [48] Sidi Yang, Tianhe Wu, Shuwei Shi, Shanshan Lao, Yuan Gong, Mingdeng Cao, Jiahao Wang, and Yujiu Yang. Maniqa: Multi-dimension attention network for no-reference image quality assessment. In *Proceedings of the IEEE/CVF conference on computer vision and pattern recognition*, pages 1191–1200, 2022. 6
- [49] Tao Yang, Rongyuan Wu, Peiran Ren, Xuansong Xie, and Lei Zhang. Pixel-aware stable diffusion for realistic image super-resolution and personalized stylization. In *European conference on computer vision*, pages 74–91. Springer, 2024. 2
- [50] Wenming Yang, Xuechen Zhang, Yapeng Tian, Wei Wang, Jing-Hao Xue, and Qingmin Liao. Deep learning for single image super-resolution: A brief review. *IEEE Transactions on Multimedia*, 21(12):3106–3121, 2019. 1
- [51] Fanghua Yu, Jinjin Gu, Zheyuan Li, Jinfan Hu, Xiangtao Kong, Xintao Wang, Jingwen He, Yu Qiao, and Chao Dong. Scaling up to excellence: Practicing model scaling for photo-realistic image restoration in the wild. In *Proceedings of the IEEE/CVF conference on computer vision and pattern recognition*, pages 25669–25680, 2024. 2
- [52] Fanghua Yu, Jinjin Gu, Zheyuan Li, Jinfan Hu, Xiangtao Kong, Xintao Wang, Jingwen He, Yu Qiao, and Chao Dong. Scaling up to excellence: Practicing model scaling for photo-realistic image restoration in the wild. In *Proceedings of*

- the IEEE/CVF conference on computer vision and pattern recognition*, pages 25669–25680, 2024. 6
- [53] Zongsheng Yue, Jianyi Wang, and Chen Change Loy. Resshift: Efficient diffusion model for image super-resolution by residual shifting. *Advances in Neural Information Processing Systems*, 36:13294–13307, 2023. 2, 7
- [54] Zongsheng Yue, Kang Liao, and Chen Change Loy. Arbitrary-steps image super-resolution via diffusion inversion. In *Proceedings of the Computer Vision and Pattern Recognition Conference*, pages 23153–23163, 2025. 2, 3, 7
- [55] Kai Zhang, Jingyun Liang, Luc Van Gool, and Radu Timofte. Designing a practical degradation model for deep blind image super-resolution. In *Proceedings of the IEEE/CVF international conference on computer vision*, pages 4791–4800, 2021. 1
- [56] Lvmin Zhang, Anyi Rao, and Maneesh Agrawala. Adding conditional control to text-to-image diffusion models. In *Proceedings of the IEEE/CVF international conference on computer vision*, pages 3836–3847, 2023. 1
- [57] Richard Zhang. Making convolutional networks shift-invariant again. In *International conference on machine learning*, pages 7324–7334. PMLR, 2019. 4
- [58] Richard Zhang, Phillip Isola, Alexei A Efros, Eli Shechtman, and Oliver Wang. The unreasonable effectiveness of deep features as a perceptual metric. In *Proceedings of the IEEE conference on computer vision and pattern recognition*, pages 586–595, 2018. 5, 6
- [59] Weixia Zhang, Guangtao Zhai, Ying Wei, Xiaokang Yang, and Kede Ma. Blind image quality assessment via vision-language correspondence: A multitask learning perspective. In *Proceedings of the IEEE/CVF conference on computer vision and pattern recognition*, pages 14071–14081, 2023. 6
- [60] Tong Zhou, Changxing Ding, Shaowen Lin, Xinchao Wang, and Dacheng Tao. Learning oracle attention for high-fidelity face completion. In *Proceedings of the IEEE/CVF Conference on Computer Vision and Pattern Recognition*, pages 7680–7689, 2020. 1

OMGSR: You Only Need One Mid-timestep Guidance for Real-World Image Super-Resolution

Supplementary Material

6. Extend Flow Matching to OMGSR

Flow Matching (FM). Unlike the DDPM scheduler, the FM scheduler maps t into $\sigma_t \in (0, 1)$ using a non-uniform spacing (e.g. the shift strategies used in FLUX models). The pre-trained noisy latent distribution \mathbf{z}_t of FM can be interpolated by \mathbf{z}_0 and ϵ :

$$\text{FM} : \mathbf{z}_t = \underbrace{(1 - \sigma_t) \cdot \mathbf{z}_H}_{\text{Signal}} + \underbrace{\sigma_t \cdot \epsilon}_{\text{Noise}}. \quad (16)$$

In practical implementation, FM follows DDPM’s formulation for consistency, deviating from the original paper. The FM objective loss is

$$\mathcal{L}_{\text{FM}} = \|\epsilon_\theta(\mathbf{z}_t, t, c) - (\epsilon - \mathbf{z}_H)\|_2^2, \quad (17)$$

where θ is typically optimized by a DiT-based model ϵ_θ .

Signal-to-Noise Ratio (SNR). FM-based models also involve a pre-trained noisy latent representation \mathbf{z}_t at timestep t , which is a linear combination of Gaussian noise ϵ and the HQ image latent representation \mathbf{z}_H . The SNR of \mathbf{z}_t is:

$$\text{FM} : \text{SNR}(\mathbf{z}_t) = \frac{(1 - \sigma_t)^2 \cdot \mathbb{E}[\mathbf{z}_H^2]}{\sigma_t^2 \cdot \mathbb{E}[\epsilon^2]} = \frac{(1 - \sigma_t)^2 \cdot \mathbb{E}[\mathbf{z}_H^2]}{\sigma_t^2}, \quad (18)$$

where $\epsilon \sim \mathcal{N}(0, I)$ and $\mathbb{E}[\epsilon^2] = 1$.

Average Optimal Mid-timestep. Similar to Sec. 3.3.2, the average optimal mid-timestep of the FM noisy latent representation can be pre-computed as:

$$\text{FM} : t^* = \arg \min_t \frac{1}{N} \sum_i \left| \text{SNR}(\mathbf{z}_t^{(i)}) - \text{SNR}(\mathbf{z}_L^{(i)}) \right|, \quad (19)$$

Note. When we precompute the t^* of the FM-based generative model and obtain \mathbf{z}_{t^*} , the subsequent training of GAN is consistent with OMGSR-S.

6.1. OMGSR-F (FLUX.1-dev)

Based on FLUX.1-dev, we develop OMGSR-F, which successfully demonstrates the compatibility of our OMGSR with FM-based generative models. Note that OMGSR-F is trained at 1K-resolution, as the default resolution for FLUX.1-dev is 1K. We obtain the average optimal mid-timestep $t^* = 244$ in FLUX.1-dev. Similar to OMGSR-S, OMGSR-F is trained on the LSDIR and FFHQ datasets. The training is conducted on dual H20 GPUs for 6000 steps with a batch size of 1, gradient accumulation of 4, and a learning rate of 5×10^{-5} . Figure 7 presents the performance

of OMGSR-F on the RealLQ250, RealSR, and DrealSR datasets. From the figure, OMGSR-F exhibits strong global and detail generation capabilities.

Note. Our OMSR framework is theoretically compatible with DDPM- and FM-based generative models, such as SD1.5, SD2.1, SD3.5, FLUX.1-dev, and the latest Qwen-Image. For different SR tasks, we can choose different foundational models to adapt them. In this paper, we will not discuss it too much.

7. Composite score on Timestep (OMGSR-S)

As stated in Sec. 4.2.1, we present the calculation of the composite score. For the maximizing metrics (i.e. CLIP-IQA, CLIPIQA+, NIMA, LIQE, MUSIQ, MANIQA), the normalized score is calculated as

$$\mathcal{S}_{\text{norm}} = \frac{\mathcal{S} - \mathcal{S}_{\text{min}}}{\mathcal{S}_{\text{max}} - \mathcal{S}_{\text{min}}}. \quad (20)$$

For the minimizing metrics (i.e. LPIPS, FID, NIEQ), the normalized score is calculated as

$$\mathcal{S}_{\text{norm}} = 1 - \frac{\mathcal{S} - \mathcal{S}_{\text{min}}}{\mathcal{S}_{\text{max}} - \mathcal{S}_{\text{min}}}. \quad (21)$$

The composite score of each test dataset is defined:

$$\mathcal{S}_{\text{comp}}^{\text{Dataset}} = \frac{\sum \mathcal{S}_{\text{norm}}^{\text{Metric}}}{\text{Metric Count}} \quad (22)$$

The average composite score of the four test datasets is defined:

$$\mathcal{S}_{\text{comp}} = \frac{\mathcal{S}_{\text{comp}}^{\text{RealSR}} + \mathcal{S}_{\text{comp}}^{\text{DrealSR}} + \mathcal{S}_{\text{comp}}^{\text{RealLQ250}} + \mathcal{S}_{\text{comp}}^{\text{RealLR200}}}{4} \quad (23)$$

We also provide the complete results in Tab. 5. From the table, the best average composite score occurs at 273 i.e. $\mathcal{S}_{\text{comp}} = (0.9793 + 0.9657 + 0.9712 + 0.9935) = 0.9774$.

8. More Qualitative Comparisons (OMGSR-S)

Figure 8 shows additional qualitative comparisons, and it can be seen that OMGSR-S achieves excellent detail representation across multiple image scenes.

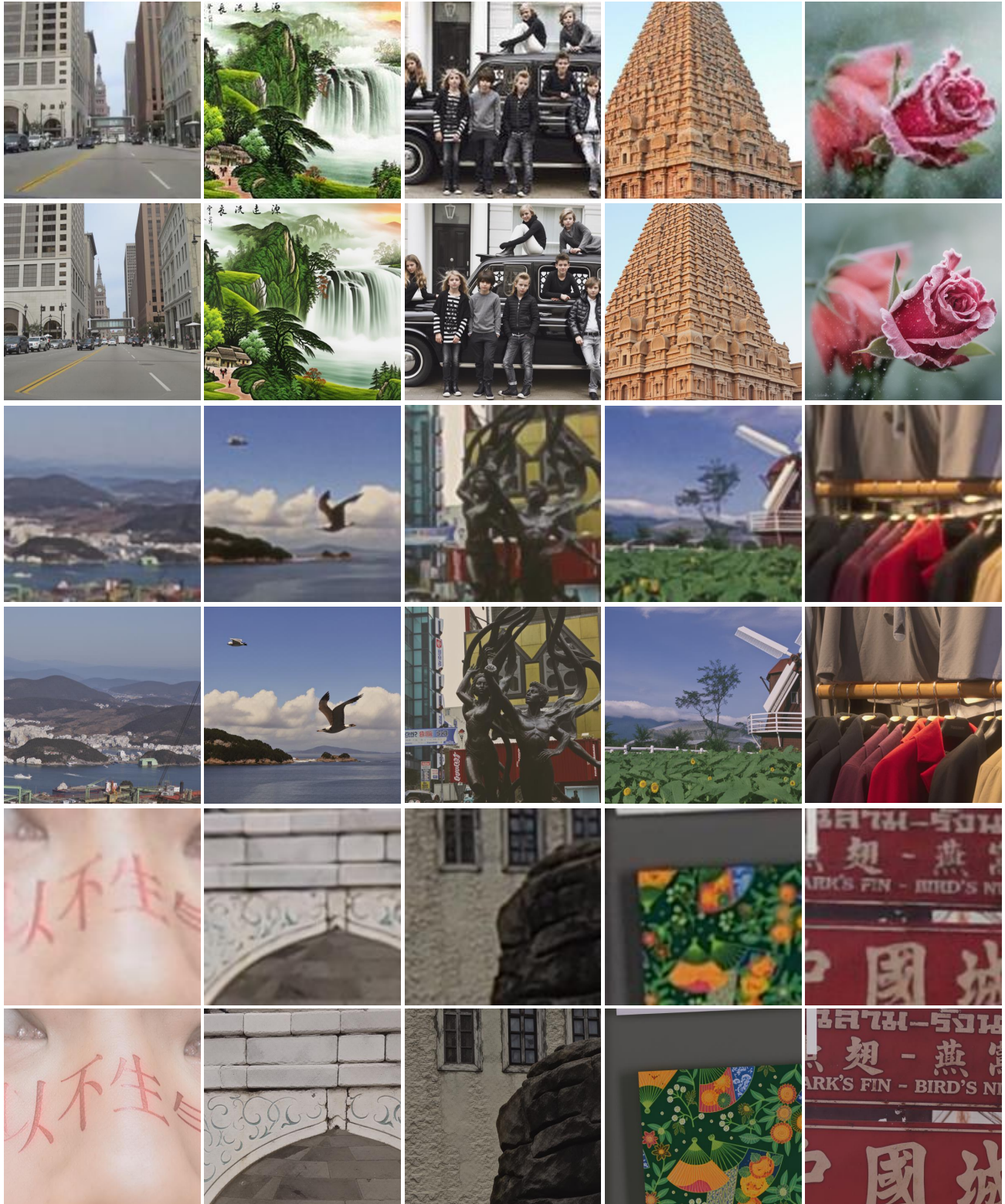


Figure 7. Visualization results of OMGSR-F. The first row is from the RealLQ250 dataset; the third row is from the RealSR dataset; the fifth line is from the DrealSR dataset. The second (256 \rightarrow 1024), fourth (128 \rightarrow 1024), and sixth (128 \rightarrow 1024) lines are images generated by OMGSR-F. Please **zoom in**.

Table 5. Ablation Study of OMGRS-S with different timesteps. We set the timestep 273 as the baseline, with intervals of 100. Note that we conduct experiments on OMGRS-S without the proposed LRR Loss to avoid any impact on the latent representation. We report a **Composite Score** based on 9 metrics across four datasets. The best and second-best results of each metric are highlighted in bold and underlined, respectively.

Datasets	Metrics	999	973	873	773	673	573	473	373	273	173	73	1
RealSR	LPIPS↓	0.4170	0.3702	0.3352	0.3003	0.2781	0.2868	0.2856	0.2788	0.2815	0.2746	<u>0.2748</u>	0.2776
	FID↓	212.50	200.89	161.65	133.99	122.77	121.16	122.34	<u>117.69</u>	117.70	117.54	118.92	125.38
	CLIPQA↑	0.2630	0.3975	<u>0.6332</u>	0.6236	0.6125	0.6254	0.6282	0.6265	0.6352	0.6184	0.6294	0.6170
	CLIPQA+↑	0.3239	0.3891	0.6448	0.6781	0.6706	0.6790	0.6766	0.6753	<u>0.6785</u>	0.6737	0.6775	0.6735
	NIMA↑	3.9255	4.5271	5.0184	<u>4.9240</u>	4.8792	4.9174	4.9153	4.8934	4.9030	4.8866	4.8638	4.8479
	NIQE↓	7.9143	5.9296	5.9524	5.7239	5.7955	<u>5.6473</u>	5.6115	5.7276	5.6487	5.7333	5.6939	5.6876
	LIQE↑	1.1054	2.1472	4.0819	4.1027	4.0200	<u>4.1557</u>	4.1047	4.1279	4.1373	4.1386	4.1745	4.1151
	MUSIQ↑	37.7757	53.6943	68.2292	68.5141	68.1226	68.1545	68.2329	68.5897	<u>68.5648</u>	68.1914	68.2788	68.1661
	MANIQA↑	0.3534	0.4158	0.6230	0.6610	0.6697	<u>0.6721</u>	0.6706	0.6712	0.6756	0.6711	0.6703	0.6500
Composite Score↑	0.0	0.3842	0.8506	0.9341	0.9494	0.9679	0.9669	0.9713	0.9793	0.9698	<u>0.9734</u>	0.9478	
DrealSR	LPIPS↓	0.3760	0.3671	0.3430	0.3122	0.2931	0.3047	0.3076	0.3046	0.3027	<u>0.2998</u>	0.3025	0.3018
	FID↓	212.27	202.16	183.24	150.05	<u>134.97</u>	138.40	135.53	138.61	132.77	137.90	139.04	145.07
	CLIPQA↑	0.3044	0.4161	0.5974	0.6346	0.6245	0.6539	0.6565	<u>0.6584</u>	0.6552	0.6491	0.6640	0.6569
	CLIPQA+↑	0.3287	0.4042	0.5852	0.6448	0.6381	0.6659	0.6505	0.6610	0.6650	0.6595	<u>0.6661</u>	0.6672
	NIMA↑	3.7182	4.3704	4.6844	4.6728	4.6659	4.7237	4.7080	4.7061	4.7416	<u>4.7303</u>	4.7125	4.6954
	NIQE↓	8.7497	6.2222	6.5924	6.6827	6.5815	6.6154	6.4873	6.5317	6.5184	6.7222	6.5704	<u>6.3530</u>
	LIQE↑	1.1721	2.5310	3.7494	3.8657	3.8151	3.8832	3.9936	3.9849	3.9885	4.0250	4.0618	<u>4.0270</u>
	MUSIQ↑	36.8816	52.5906	62.4311	63.6773	63.2950	64.9613	65.1226	65.0771	<u>65.3381</u>	65.0661	65.6084	65.2814
	MANIQA↑	0.3679	0.4163	0.5700	0.6023	0.6160	0.6210	0.6234	0.6244	0.6259	<u>0.6277</u>	0.6285	0.6039
Composite Score↑	0.0	0.4009	0.7434	0.8799	0.9274	0.9412	0.9469	0.9484	0.9657	0.9497	<u>0.9598</u>	0.9451	
RealLQ250	CLIPQA↑	0.2994	0.4472	0.5647	0.6503	0.6570	0.6945	0.6931	0.6938	0.6976	<u>0.6952</u>	0.6946	0.6908
	CLIPQA+↑	0.3716	0.4657	0.5949	0.6800	0.6836	0.7052	0.7005	0.7017	<u>0.7065</u>	0.7073	0.7012	0.7025
	NIMA↑	4.5873	5.2518	<u>5.1600</u>	5.0815	5.1142	5.1088	5.1168	5.0935	5.1490	5.1254	5.1224	5.1324
	NIQE↓	7.2817	4.4344	4.4566	4.1618	3.9151	4.1169	4.0448	4.1001	<u>4.0240</u>	4.0927	4.1152	4.0679
	LIQE↑	1.1207	2.2094	3.1658	3.7760	3.7987	<u>3.9796</u>	3.9433	3.9234	3.9954	3.8639	3.8418	3.8582
	MUSIQ↑	43.9835	54.3022	63.0905	67.6347	68.3741	69.5356	69.6991	<u>69.7241</u>	69.8671	69.1404	69.4704	69.2748
	MANIQA↑	0.3304	0.3749	0.5446	0.6084	0.6175	0.6255	0.6339	0.6302	0.6302	<u>0.6308</u>	0.6290	0.6139
	Composite Score↑	0.0	0.4887	0.7411	0.8891	0.9200	0.9521	<u>0.9574</u>	0.9483	0.9712	0.9524	0.9479	0.9439
	RealLQ200	CLIPQA↑	0.2996	0.4508	0.5997	0.6550	0.6641	0.6962	0.6944	0.6920	0.7016	0.6971	<u>0.7001</u>
CLIPQA+↑		0.3740	0.4762	0.6282	0.6953	0.7017	0.7197	<u>0.7205</u>	0.7198	0.7211	0.7202	0.7201	0.7162
NIMA↑		4.4772	5.0967	5.3409	5.2591	5.2736	5.2953	5.3173	5.3153	5.3617	<u>5.3425</u>	5.3363	5.3243
NIQE↓		7.2073	4.4231	4.5819	4.2892	4.2503	4.1507	4.1882	4.1302	<u>4.0731</u>	4.1353	4.1780	3.9494
LIQE↑		1.1756	2.2239	3.5141	3.9733	4.0361	4.1637	4.1497	<u>4.1688</u>	4.1901	4.1684	4.1513	4.1417
MUSIQ↑		43.1193	55.2588	63.9919	67.3852	68.5206	69.6565	69.7687	69.7503	69.8960	69.1132	69.4267	<u>69.8007</u>
MANIQA↑		0.3448	0.4000	0.5859	0.6368	0.6477	0.6527	0.6537	0.6567	<u>0.6571</u>	0.6594	0.6529	0.6449
Composite Score↑		0.0	0.4574	0.7975	0.9074	0.9313	0.9724	0.9744	0.9776	0.9935	<u>0.9816</u>	0.9776	0.9768
Average Composite Score↑		0.0	0.4328	0.7831	0.9026	0.932	0.9584	0.9614	0.9614	0.9774	<u>0.9634</u>	0.9647	0.9534

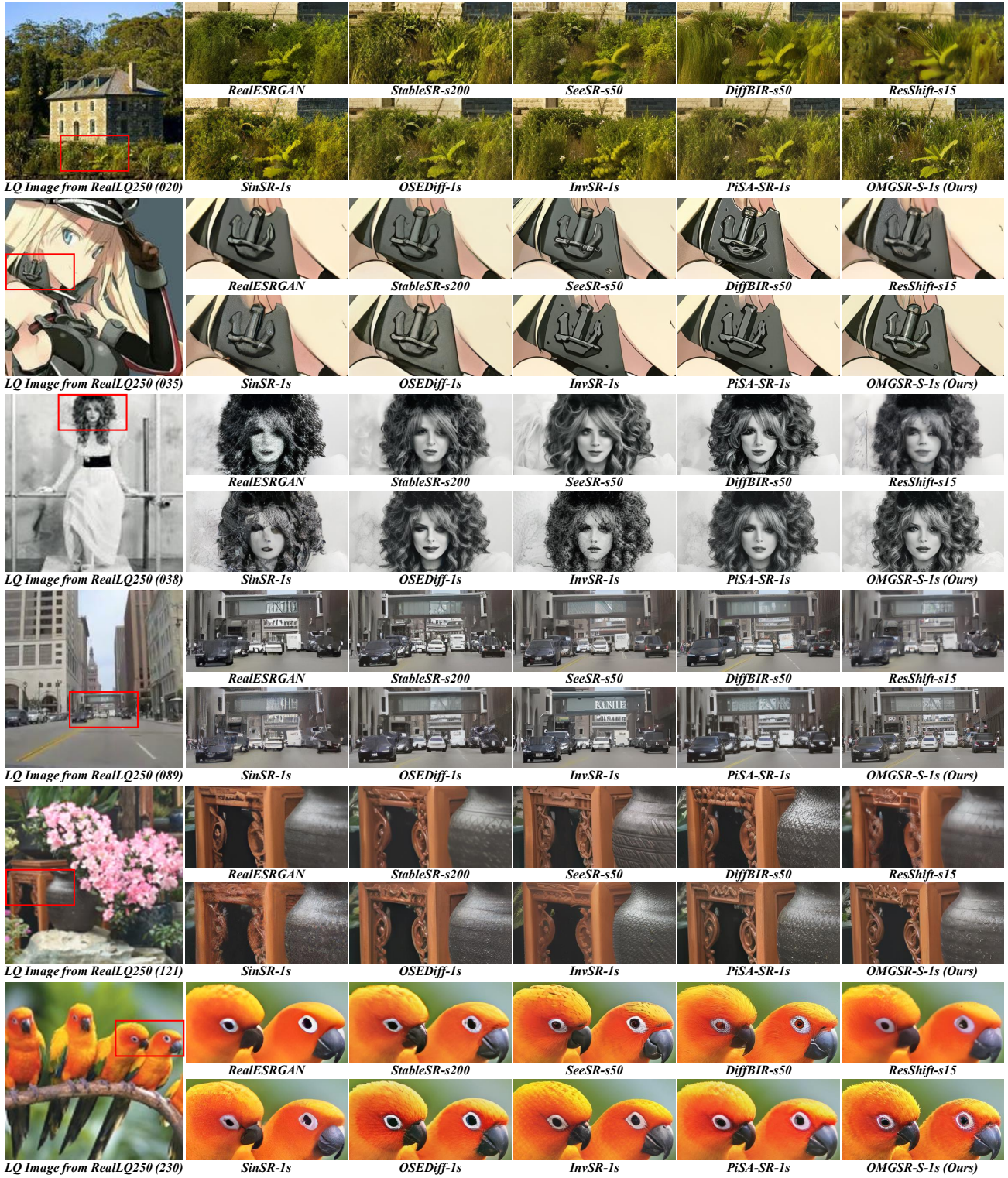


Figure 8. Qualitative comparisons with state-of-the-art multi-step and one-step models on RealLQ250. Please **zoom in**.